END
DATE
FILMED

7 80

DTIC

1.0

1.1

1.25 1.4 1.6

2.8 2.5
3.2 2.2
3.6
4.0 2.0

1.8

MICROCOPY RESOLUTION TEST CHART
NATIONAL BUREAU OF STANDARDS 1963-A
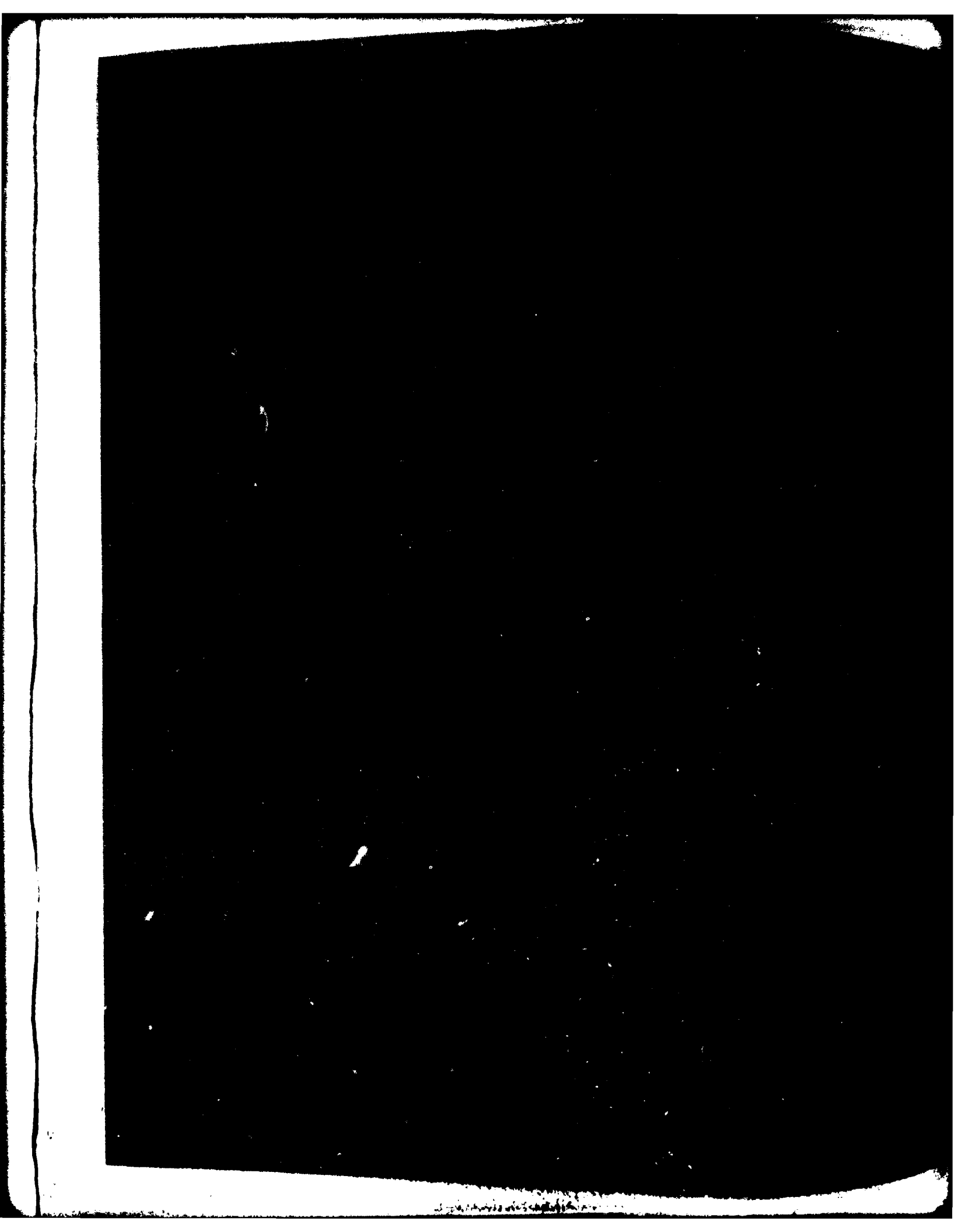
Interim rept. 1 May 78-1 Apr 79

REPORT DOCUMENTATION PAGE		READ INSTRUCTIONS BEFORE COMPLETING FORM
1. REPORT NUMBER AFWAL-TR-80-1027	2. GOVT ACCESSION NO. AD-A085 754	3. RECIPIENT'S CATALOG NUMBER
4. TITLE (and Subtitle) HIGH DENSITY MAGNETIC BUBBLE MEMORY TECHNIQUES		5. TYPE OF REPORT & PERIOD COVERED 1 MAY 1978 to 1 APRIL 1979 Interim
		6. PERFORMING ORG. REPORT NUMBER C76-845.47/501
7. AUTHOR(s) D. M. HEINZ V. SPERIOSU		8. CONTRACT OR GRANT NUMBER(s) F33615-76-C-1198
9. PERFORMING ORGANIZATION NAME AND ADDRESS ROCKWELL INTERNATIONAL ELECTRONICS RESEARCH CENTER P.O. BOX 4761, ANAHEIM, CA 92803		10. PROGRAM ELEMENT, PROJECT, TASK AREA & WORK UNIT NUMBERS 6096-20-07
11. CONTROLLING OFFICE NAME AND ADDRESS AVIONICS LABORATORY (AADE) AF WRIGHT AERONAUTICAL LABORATORIES (AFSC) WRIGHT-PATTERSON AFB, OHIO 45433		12. REPORT DATE March 1980
		13. NUMBER OF PAGES 24
14. MONITORING AGENCY NAME & ADDRESS(if different from Controlling Office)		15. SECURITY CLASS. (of this report) UNCLASSIFIED
		15a. DECLASSIFICATION DOWNGRADING SCHEDULE

16. DISTRIBUTION STATEMENT (of this Report)

APPROVED FOR PUBLIC RELEASE: DISTRIBUTION UNLIMITED

17. DISTRIBUTION STATEMENT (of the abstract entered in Block 20, if different from Report)

18. SUPPLEMENTARY NOTES

19. KEY WORDS (Continue on reverse side if necessary and identify by block number)

BUBBLE GARNET MATERIAL
ION IMPLANTATION
X-RAY DIFFRACTION

20. ABSTRACT (Continue on reverse side if necessary and identify by block number)

Ion implantation of device structures into magnetic garnet films is a developing technique for producing bubble memory devices. In order to specify the implantation species, energy and dose, it is necessary to know the effect that these implantation conditions have on the garnet's crystalline and magnetic properties. A kinematical model of X-ray diffraction was developed for a thin layer whose strain and damage distributions are functions of depth. The actual strain and damage

DD FORM 1473 1 JAN 73 EDITION OF 1 NOV 65 IS OBSOLETE

407112

distributions in ion-implanted layers may be obtained by fitting experimental X-ray diffraction rocking curves. Synthesis of the distributions is greatly facilitated by taking a rocking curve after each of a series of progressively deeper etching steps. A detailed description of the kinematical model is followed by its application to implanted garnet, and results are presented for single and multiple ion implantations.

This is the fourth Interim Technical Report on Contract F33615-76-C-1198, covering the contract period of 1 May 1978 to 1 April 1979. The first interim report, AFAL-TR-77-17, covers the period 4 May 1976 to 4 November 1976; the second interim report, AFAL-TR-77-198, covers the period 4 November 1976 to 4 May 1977; the third interim report, AFAL-TR-78-31, covers the period of 4 May 1977 to 4 November 1977.

The reported work was performed in the Bubble Memory Technology Department, Electronics Research Center, Rockwell International Corporation, Anaheim, CA. Dr. G. R. Pulliam is Department Director and Program Manager of this contract. D. M. Heinz is Principal Investigator. V. S. Speriosu is the major contributor to this report.

On 1 May 1978, a study was initiated on the physics of ion-implantation in magnetic garnets with the aim of determining requirements for simple propagation structures in contiguous disk types of bubble memory devices. After work on this contract task ended, the investigation was continued on a Rockwell International internally-funded program. During this period, the use of ferromagnetic resonance measurements were developed to complement the X-ray diffraction techniques evolved earlier. The combined results of the contract-supported and Rockwell supported studies are presented in this document to provide a complete account of this investigation.

The contractor's report number is C76-845.47/501.

Accession For	
NTIS GRA&I	☑
DDC TAB	☐
Unannounced	☐
Justification____	
By____	
Distribution/	
Availability Codes	
Dist	Avail and/or special
A	

TABLE OF CONTENTS

LIST OF ILLUSTRATIONS

SECTION I

INTRODUCTION

The objective of this research effort is to demonstrate the feasibility of a new technology for all solid state large data base memories for airborne/spaceborne applications. The program scope is limited to demonstrating the feasibility of the device functions and bit density capabilities required to meet the system goals.

It is the objective of this program to advance one technology into development. Based on an evaluation of the present and potential capabilities of candidate solid state technologies to meet the system goals, magnetic bubble domain technology has been selected as the one to be pursued on this program.

As the bubble device period of a permalloy propagation structure is scaled down to attain higher bit densities, two serious problems arise: one is related to photolithographic resolution and the other is related to in-plane magnetic drive field. Currently, the most advanced permalloy propagation structure is the asymmetric chevron whose minimum feature is about one eighth of the circuit period. Since the limit of optical photolithographic resolution is $\geqslant 1\mu m$, a $4\mu m$ period device must be fabricated by some other lithographic technique such as electron beam microfabrication. The minimum drive field of a permalloy device is proportional to the magnetization of the bubble material (which is approximately inversely proportional to the bubble diameter). As a result, the drive field of a permalloy device increases rapidly with decreasing bubble diameter. Existing $8\mu m$ period permalloy devices, though not optimized, require more than 60 Oe operating drive field. Thus, even when the electron beam microfabrication technique becomes available, the expected increase in drive field casts some doubt on the viability of $4\mu m$ period permalloy devices.

The ion-implanted contiguous disk device appears to solve both of the above-mentioned problems. As far as the propagation structure is concerned, the minimum feature of an ion-implanted device can be increased by a factor of three (or more) over that of the asymmetric chevron, which makes possible the fabrication of a $4\mu m$ period device by conventional photolithography. In contrast to the permalloy device, the ion-implanted device has no circuit gaps along its propagation track. Consequently, the energy of a bubble is nearly independent of its position along the propagation track, resulting in a very weak dependence of the minimum drive field on the garnet magnetization. Thus, both the lithographic resolution and the high drive field problems of $4\mu m$ period permalloy devices may be solved by ion-implanted devices.

1

Ion-implantation is an established technique for changing some of the properties of as-grown crystals, having been successfully applied to both semiconductors and garnets (Ref 1). In recent years, ion-implantation has assumed a key role in the treatment of magnetic bubble materials for hard bubble suppression (Ref 2), as well as in the development of contiguous disk bubble memory devices (Ref 3). Although widely used, the effects of ion-implantation are not very well understood. No a priori guidelines for selecting optimum implantation conditions are available. For contiguous disk devices, the final test is device performance, characterized by minimum drive field and maximum bias margin. Since the trial-and-error approach for optimizing implantation by preparing processed devices would be prohibitively time consuming and expensive, the more fundamental approach of investigating the physics of ion-implanted garnet was adopted.

A study was initiated on this program to determine the dependence of the garnet's crystalline and magnetic properties on ion-implantation conditions: Species, energy, dose and temperature. One of the major macroscopic changes in the crystal structure is the expansion of the unit cell, which places the implanted garnet in compressive stress. In bubble materials with a negative magnetostriction constant, the stress induces a negative magnetic anisotropy field, H_k, whose value and depth dependence greatly influence device performance. The microscopic displacement of atoms from their perfect-crystal positions, usually termed implantation damage, affects other magnetic properties such as magnetization, $4\pi M_s$, coercivity, H_c, exchange constant, A, and gyromagnetic ratio, γ. Knowledge and control of these properties and of their stability over a wide temperature range are essential to device manufacture.

Several methods are presently in use for the study of ion-implantation: The rate of chemical etching is known to depend on the extent of damage (Ref 4), the presence of additional absorption peaks in spin-wave resonance is interpreted as an indication of a layer with negative anisotropy (Refs 5, 6), changes in magnetic bubble collapse fields are used as a rough measure of the implantation-induced flux-keeper effect (Ref 7), and both the Rutherford-scattered ion flux (Ref 8) and low energy electron diffraction (Ref 9) are related to lattice structural changes. Although each method has proved useful in understanding implanted crystals, their common feature is the difficulty in obtaining detailed and quantitative interpretations of experimental results.

Double crystal X-ray diffraction has also been applied to the study of ion-implanted materials (Refs 10,11,12). Diffraction profiles (rocking curves) contain information about the small changes in lattice parameters (strain), microscopic displacement (damage), and other inhomogeneities caused by implantation. A method of extracting this information from experimental rocking curves has been developed on this program and has been used successfully on implanted garnet, as described in later Sections (Ref 13). The method is general and applicable not only to implanted crystals, but also

2

to diffused or as-grown crystals whose crystallographic properties vary with depth. The relative simplicity of the experimental technique and mathematical treatment should make this approach accessible to a wide variety of workers.

In addition to X-ray diffraction, ferromagnetic resonance (FMR) has been used to obtain direct values for the anisotropy field, H_k, the gyromagnetic ratio, γ, the damping parameter, α, the exchange constant, A, and rough values for the magnetization, $4\pi M_s$. A method yielding the depth dependence of H_k in an ion-implanted film has been published recently[Ref 14], which showed that the profile of H_k is proportional to the strain distribution, as predicted by theory. This FMR method has been adapted as a complementary tool to our X-ray technique in analyzing ion-implanted garnets.

The remainder of this report consists of the following parts: Section II describes the kinematical model of X-ray diffraction and its application to implanted garnet; Section III presents the results and discussion of the study of Ne^+, He^+, and H^+ implantations; and Section IV summarizes the results of this investigation.

3

SECTION II

KINEMATICAL X-RAY DIFFRACTION IN THIN CRYSTALS

X-ray diffraction is a standard laboratory tool for the determination of crystal structure. In the usual double-crystal experimental set-up, the X-ray output of a metal target is collimated, monochromatized and partially polarized by a first crystal of good quality. The second (sample) crystal, whose lattice parameters are to be measured, is slowly rotated with respect to the incident X-ray beam, while the diffracted beam intensity is monitored. The intensity profile as a function of angle is called a rocking curve. Figure 1(a) schematically shows the rocking curve of a thick crystal with uniform lattice constant. The intensity is zero except for the narrow angular range which satisfied the Bragg condition. The position of the peak is determined by the lattice parameter of the as-grown crystal, (in this case, an epitaxial garnet film grown by liquid phase epitaxy, LPE). The width and detailed shape of the peak indicate the degree of uniformity and perfection of the crystal.

After ion-implantation (by appropriate implantation species, energies, and dosages), an increase in diffracted beam intensity is observed on the low angle side of the LPE peak. As shown in Figure 1(b), this intensity has an oscillatory character and is typically 10 to 100 times less than the LPE peak. The period of oscillation varies, but is always greater than the width of the LPE peak. Since the thickness of an implanted layer is small compared to both extinction and absorption lengths[Ref 15], a kinematical model of diffraction is valid[Ref 16]. In this section we show how a kinematical treatment of the diffraction problem can account for the detailed shape and intensity of the implanted layer rocking curve. By adopting this approach, quantitative values for the strain and damage distributions may be obtained, and consequently, the thickness of ion-implanted layer.

Kinematical theory deals with weakly reflecting planes of spacing, d, (which is not necessarily constant throughout the crystal). The calculation of the total reflected amplitude consists of the addition of the plane wave amplitudes, reflected (only once) by each plane, with proper account taken of the phases. Simplifications result if the planes are parallel and infinite in extent. Disorder in the crystal lattice is introduced in a manner similar to the Debye-Waller treatment of thermal fluctuations, i.e., by decreasing the reflectivity of each plane. This is equivalent to a decrease in the structure factor of a given reflection.

The strain and damage distributions in ion-implanted crystals have been found to vary only with depth, being constant and isotropic at a given distance from the surface. At any depth, the strain perpendicular to the surface is defined as the fractional change in the spacing between planes parallel to the surface, $(d-d_0)/d_0$, where d is the strained spacing and d_0 is the undisturbed spacing. Except for very high implantation dosages, when amorphous layers may be created, the constraints imposed by the unaffected, bulk (film and substrate) crystal cause the strain parallel to

4

LPE Peak

Angle →
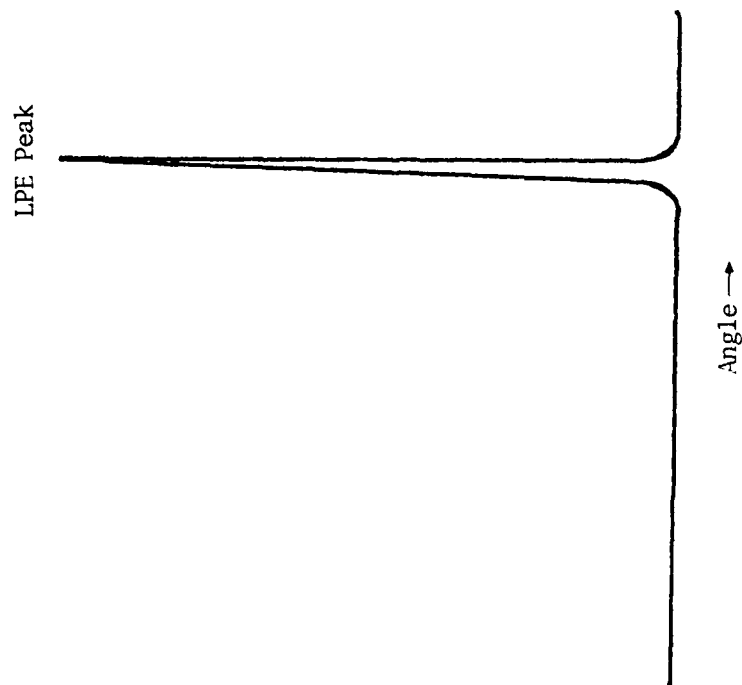
(a) Before ion implantation

LPE Peak

Intensity Due to
Implanted Layer X100

Angle →
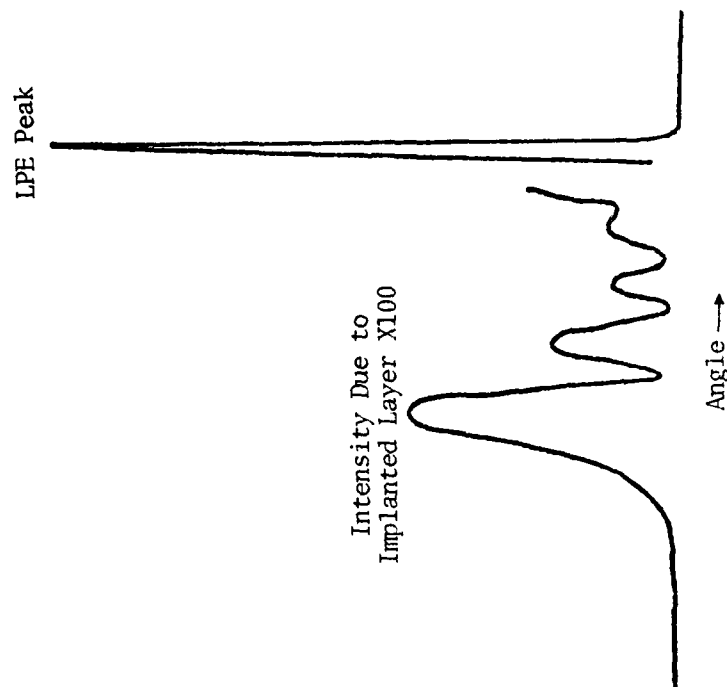
(b) After ion implantation. (The separation
between the largest implanted layer peak
and the LPE peak is about 0.3 degrees.)

Figure 1. X-ray Rocking Curves Showing Diffraction Profiles of an
LPE Garnet Film Before and After Ion Implantation.

5

the surface to be much less than that perpendicular to the surface.

The effects of ion-implantation are represented in our model by an arbitrary number, N, of laminae parallel to the surface. Each lamina, j, has its own number of planes, n_j, inter-planar spacing, d_j, and damage function, W_j. The damage function varies from zero (amorphous layer) to one (perfect crystal). The condition for the validity of a kinematical approach is that the thickness of any lamina i, $n_i d_i$, be much less than L_O, the extinction length. If the total thickness is much less than the absorption length, ℓ_O, absorption may be safely neglected. For garnets, typical values of L_O and ℓ_O in strong reflection are 2μm and 10μm, respectively.

For unit incident amplitude and σ-polarization, the complex amplitude reflected by an undamaged plane(Ref 17) is given by

$$q = -i \frac{d_o}{V \sin\theta_B} \frac{\lambda}{} \frac{e^2}{mc^2} |F_{hk\ell}| \tag{1}$$

where d_o = undisturbed inter-planar spacing; λ = X-ray wavelength; V = volume of unit cell; θ_B = Bragg angle of undisturbed crstal; e^2/mc^2 = classical electron radius; $F_{hk\ell}$ = structure factor for reflection (hkℓ).

The total amplitude reflected by the N laminae, obtained by summing the amplitudes coming from individual planes, account being taken of phase differences and damage, is given by

$$A_N = q \sum_{j=1}^{N} W_j e^i [(n_j - 1)\frac{\delta_j}{2} + \phi_j] \frac{\sin n_j \frac{\delta_j}{2}}{\sin \frac{\delta_j}{2}} \tag{2}$$

where $1-W_j$ = damage of lamina j;

$$\delta_j = \frac{4\pi}{\lambda} \epsilon d_o \cos \theta_B + 2\pi \frac{\Delta d_j}{d_o} ;$$

$\epsilon = \theta - \theta_B$ = angle relative to Bragg angle;

$\Delta d_j = d_j - d_o ;$

$$\phi_j = \sum_{i=1}^{j-1} n_i \delta_i ; \phi_1 = 0 .$$

6

In symmetric reflections and for $\theta_B < \pi/4$, the amplitude at the surface of a thick perfect crystal (derived from Ref 15, Eq. 35.1) is

$$\chi = \frac{1}{2p} \left[1 + \frac{1}{4p^3} \right] \, , \, p \gg 1 \tag{3}$$

where

$$p = - \frac{\sin 2\theta_B}{|C| \, \dfrac{e^2}{mc^2}} \, \frac{\pi}{\lambda^2 |\Gamma_{hk\ell}|} \, \frac{\epsilon}{} \, V$$

and

$$C = 1 \text{ for } \sigma\text{-polarization or } \cos 2\theta \text{ for } \pi\text{-polarization.}$$

Experimentally, it is found that the Bragg peak reflected by the bulk LPE crystal is broader and less intense than the predictions of the perfect crystal dynamical theory. This is probably due to composition and lattice parameter variations. In the angular range of interest, corresponding to the tail of the Bragg peak, this discrepancy can be eliminated by fitting the measured bulk intensity with a function, such as an exponential, and using its square root as the bulk amplitude. A good fit can usually be obtained by simply multiplying the theoretical perfect crystal amplitude by a fitting factor, f, whose value (between 1 and 3) is chosen for the best agreement. This procedure is legitimate since we are not interested in a theoretical model for the bulk.

Neglecting multiple reflections between the ion-implanted layer and the bulk, for unit incident amplitude and σ-polarization, the total reflected amplitude becomes

$$R(\epsilon) = A_N(\epsilon) + f \, \chi(\epsilon) \, e^{-i\delta_1} \tag{4}$$

and the intensity is

$$I(\epsilon) = |R(\epsilon)|^2$$

$$= |A_N(\epsilon)|^2 + [f \, \chi(\epsilon)]^2 + 2f \, \chi(\epsilon) \cos \delta_1 \, . \tag{5}$$

Since the incident beam is not perfectly σ-polarized by its reflection from the first crystal, the top layer amplitude, A_N, should be multiplied by $[(1 + \cos^2 2\theta_B) / (1 + \cos 2\theta_B)]^{1/2}$.

Several comments should be made at this point. The strain and damage distributions are expected to be continuous and this can be approximated by subdividing the ion-implanted layer into a large number, N, of laminae. However, due to the relatively large breadth of the Bragg peaks, (about 0.1 degrees), it is found that finer division than about 150Å per lamina does not appreciably change the calculated intensity distribution. Thus, a 1500Å-thick, ion-implanted layer can be well represented by 10 or fewer discrete laminae. By the use of a computer, the correct strain and damage distributions may be synthesized by trial and error until the intensity matches the measured rocking curve. Analytical approaches, such as Fourier-analyzing the rocking curve, are more elegant, but also more limited. By calculating the Patterson series of the rocking curves of diffused and ion-implanted layers, Afanasev, et al (Ref 16) obtained the average strain and thickness, but not the strain and damage distributions.

If the strain and damage distributions are to be synthesized by the fitting of experimental data, the sensitivity of the rocking curve to small changes in the strain and damage distributions should be examined. On theoretical grounds the rocking curve should be very sensitive to such changes. For a typical total thickness of several thousand Å, the relative phase of amplitudes originating from differently strained laminae can vary by several times π. A slight change in the strain distribution should result in drastic changes in the rocking curve. This is demonstrated in Figure 2(a) where a rocking curve (solid line) corresponding to the strain (solid line) in Figure 2(b) is plotted. The rocking curve as well as the strain and damage (dotted line) distributions are typical of 200KeV Ne^+ implants in garnet. If the strain distribution is changed by a small amount, yielding the dashed distribution in Figure 2(b), the result is a marked redistribution in the oscillations, as shown by the dashed line in Figure 2(a). The positions and the relative heights of the maxima have changed, although the total area under the curve has remained constant. A similar, but less pronounced, effect is obtained if the damage distribution is varied. These considerations indicate that a good fit of an experimental curve yields a strain distribution which is accurate to better than 5 percent at any depth. Since the rocking curve is less sensitive to damage, the accuracy for the damage distribution is only 15 percent or better.

The synthesis approach becomes very useful when rocking curves are taken after progressively deeper etching, performed in steps of 100 to 200Å. Starting with the deepest etch, the distribution in this portion of the ion-implanted layer is easily determined by one or two discrete laminae whose total thickness is fixed. The strain and damage in the next lamina are found by fitting the appropriate rocking curve without changing the distribution obtained at the previous step. In this manner, the distribution is built up from the bottom. The assumption that a given
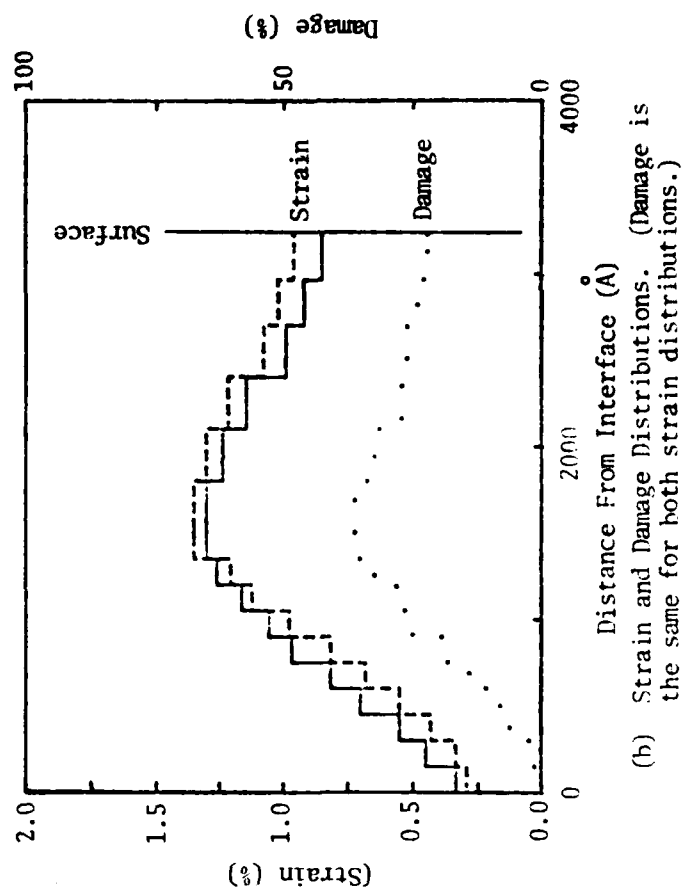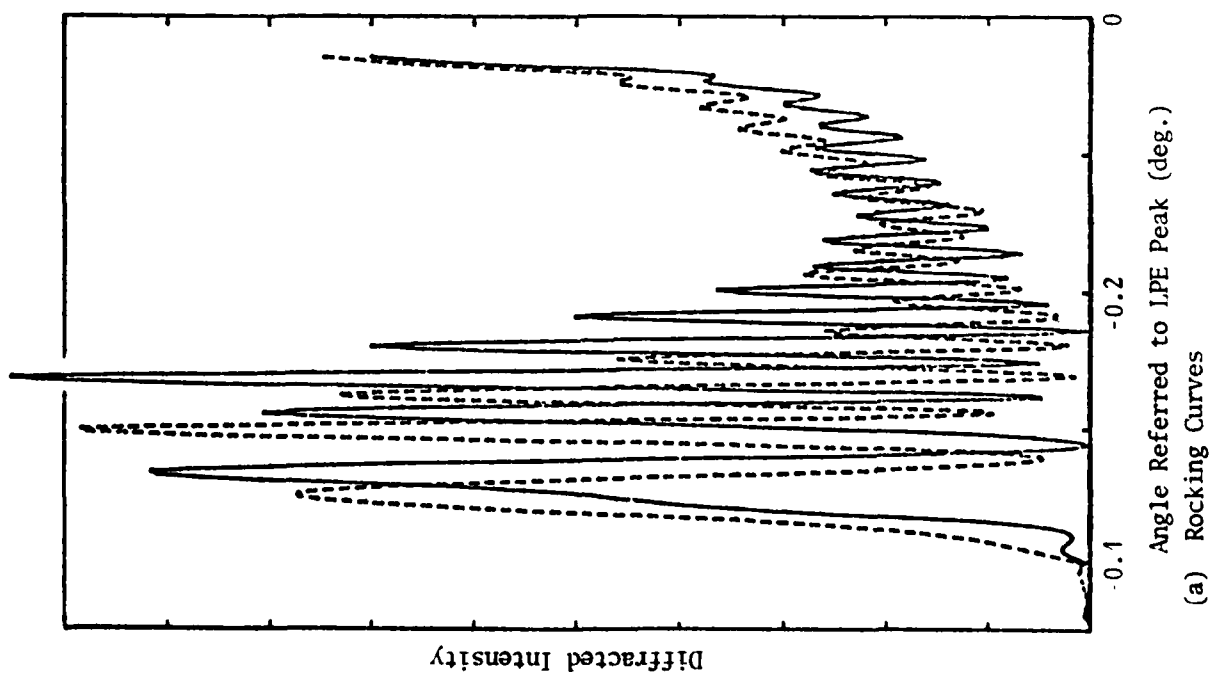
Damage (%)

(b) Strain and Damage Distributions. (Damage is the same for both strain distributions.)

(Strain %)

Figure 2. Dependence of Calculated Rocking Curve on Strain Distribution.

Diffracted Intensity

(a) Rocking Curves

6

lamina is not appreciably affected by the presence of adjacent laminae is supported by the agreement between calculated and measured rocking curves.

After some experimentation, hot concentrated nitric acid was chosen as a suitable etchant for implanted garnet. At 90°C, implanted material etch rates are in the neighborhood of 100 to 200Å/min, which provides a convenient and reproducible means for removing implanted garnet. The surface roughening caused by etching under these conditions is within tolerable limits. The thickness of implanted material removed is determined from the unimplanted etch rate (about 25Å/min at 90°C), plus a mechanical measurement of the step height which develops at the unimplanted-implanted boundary.

SECTION III

RESULTS AND DISCUSSION

This section describes the key properties of bubble materials implanted with single energy Ne^+, He^+ or H^+, as well as double and triple energy Ne^+ and He^+ combinations. These species were selected because of their widespread use for hard bubble suppression and contiguous disk device fabrication (Refs 3,12,18). The device requirement of low level of damage, uniformly-strained drive layers (Ref 3) focused the investigation on the dependence of strain and damage distributions on implant species, energy, and dose. In addition, FMR measurements of some of the samples yielded values for H_K, γ, and α.

The bubble films used were YSmLuCaGeIG with thicknesses varying between 1 and 3μm. Implantation was performed at a $1\mu A/cm^2$ dosage rate in order to minimize self-annealing effects. Multiple energy implantations were made in order of descending energy. The temperature of the samples during implantation was estimated to be between 150 and 200°C.

Figure 3 shows the (444) CuK_α rocking curves of samples implanted with 200 KeV, 120 KeV, 200 KeV + 50 KeV, and 200 KeV + 120 KeV + 50 KeV, $6x10^{13} Ne^+/cm^2$ for each energy. The curves corresponding to single-energy implantations are qualitatively the same, except that the 200 KeV curve is sharper and more intense. The bottom two curves are qualitatively different from each other as well as from the single-energy curves. The kinematical model interpretation of these and other curves in terms of strain and damage distributions is shown next.

Figure 4(a) shows the experimental and theoretical rocking curves of the 120 KeV, $6x10^{13} Ne^+/cm^2$ single implantation. The strain and damage distributions which yield the theoretical rocking curves are shown in Figure 4(b). The vertical dotted lines in this figure indicate the etch steps at which rocking curves were taken. The very good agreement between the experimental and calculated rocking curves implies that the strain and damage distributions are accurate to within a few ($\lesssim 5$) percent.

For this dosage, the damage is very low while the strain is fairly uniform. The maximum strain (0.47 percent) is at about 1000Å from the surface; this is slightly deeper than half of the implanted layer thickness (1800Å). At the layer-bulk interface and at the surface, the strain values are 0.29 percent and 0.34 percent, respectively, which gives the distribution a slightly skewed appearance.

The rocking curves and the strain and damage distributions of the 200 KeV, $6x10^{13} Ne^+/cm^2$ sample are shown in Figures 5(a) and (b), respectively. Qualitatively the distributions are the same as for the lower energy case. The important differences are in the layer thickness (3100Å) and maximum strain (0.42 percent). It appears that the 120 KeV implantation results in a slightly higher strain and damage than the 200 KeV implantation, even though the dosages are the same. This is attributed to increased straggling by higher energy implantation ions.

11

Dosage for each energy is 6×10^{13} Ne$^+$/cm^2

Implantation Energies

1. 200 KeV
2. 120 KeV
3. 200 KeV + 50 KeV
4. 200 KeV + 120 KeV + 50 KeV

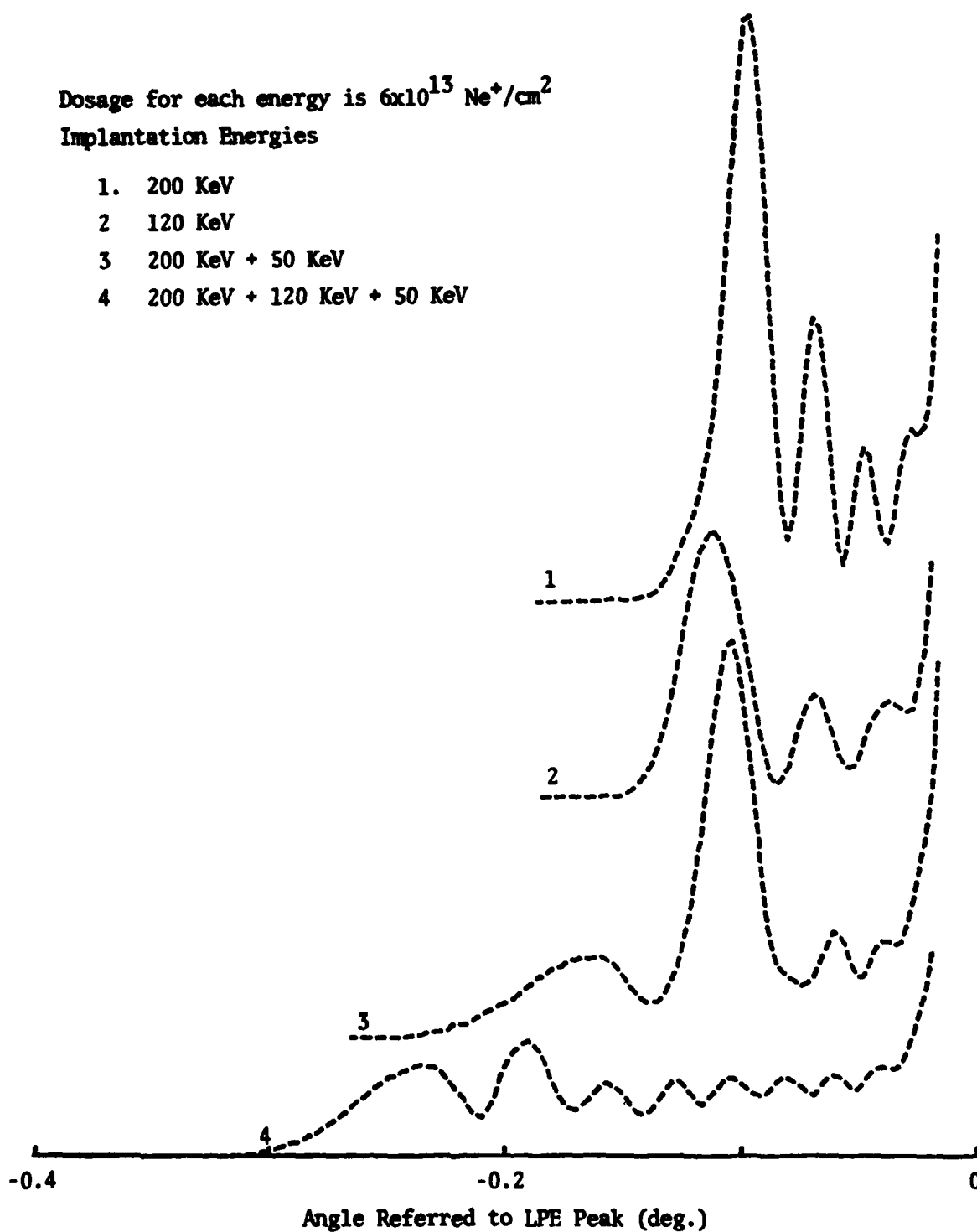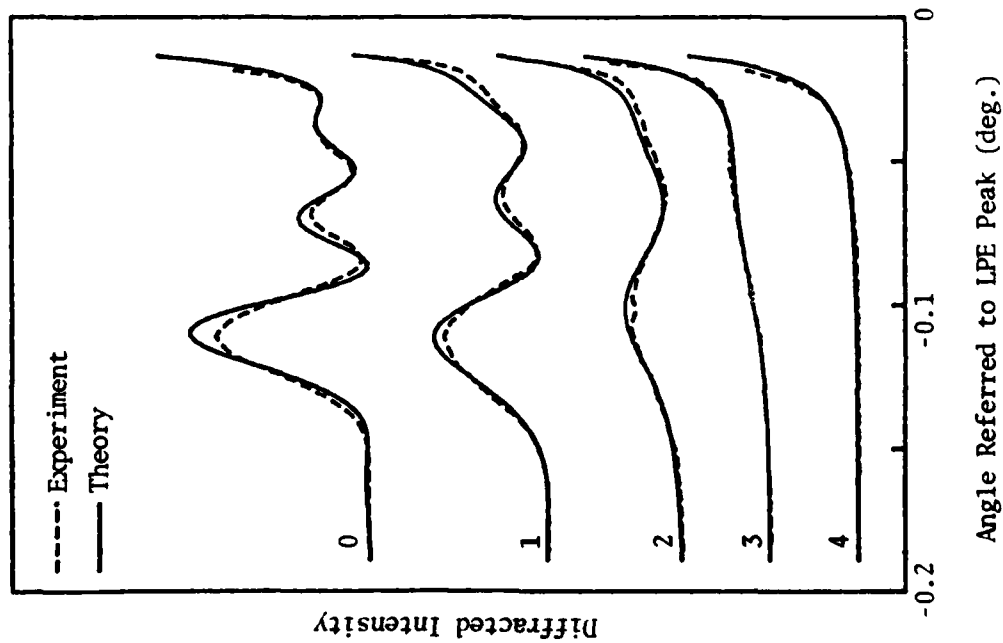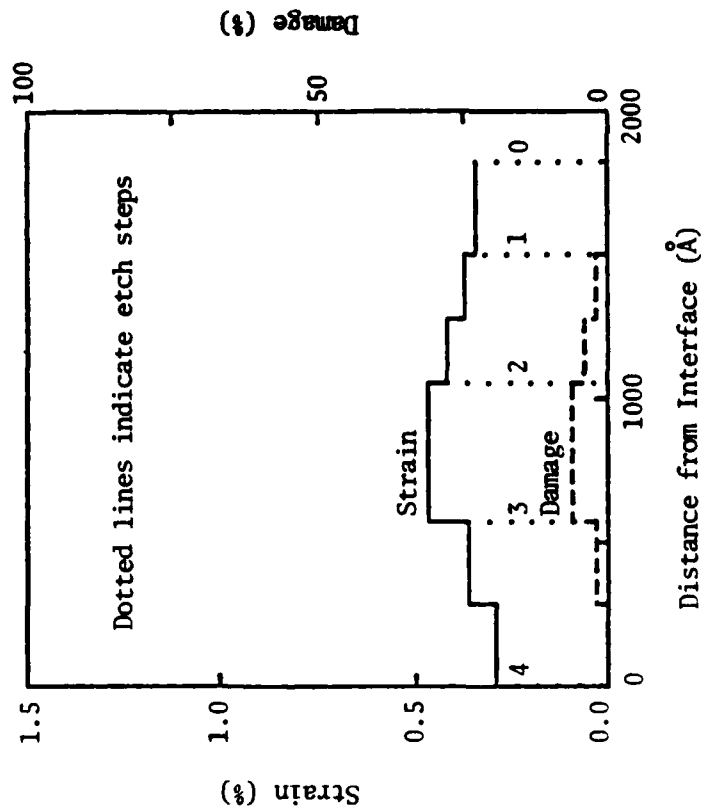Angle Referred to LPE Peak (deg.)

Figure 3. Rocking Curves Resulting from Different Single
and Multiple Implantations.

12

(b) Calculated Strain and Damage Distributions

Damage (%)

Strain (%)

Distance from Interface (Å)

Dotted lines indicate etch steps

Strain

Damage

---- Experiment
— Theory

Diffracted Intensity

Angle Referred to LPE Peak (deg.)

(a) Rocking Curves as a Function of Etching

Figure 4. Rocking Curves, and Strain and Damage Distribution for an Implantation of 120 KeV, 6×10^{13} Ne$^+$/cm^2.
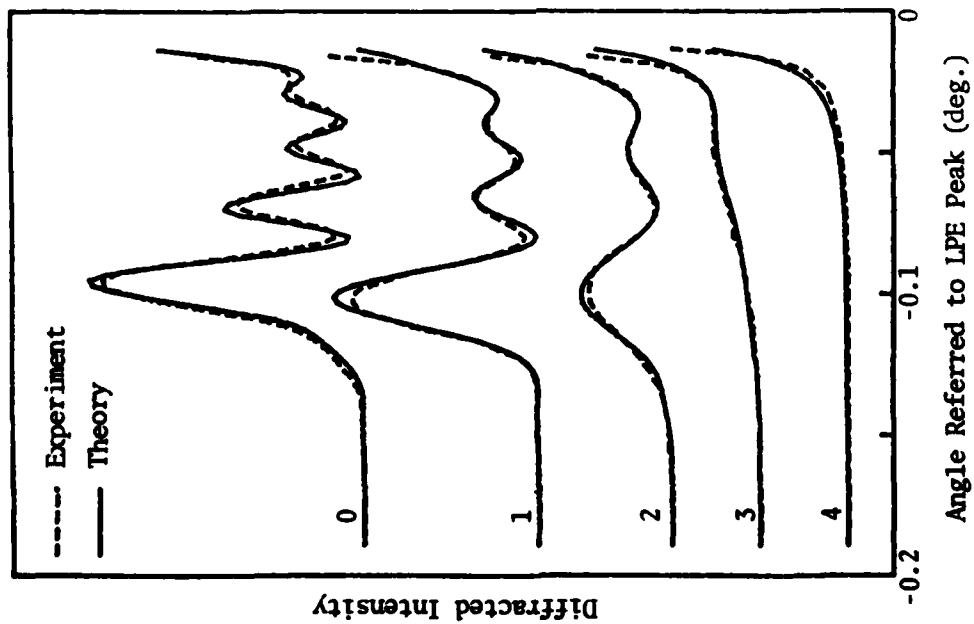
(b) Calculated Strain and Damage Distributions

(a) Rocking Curves as a Function of Etching
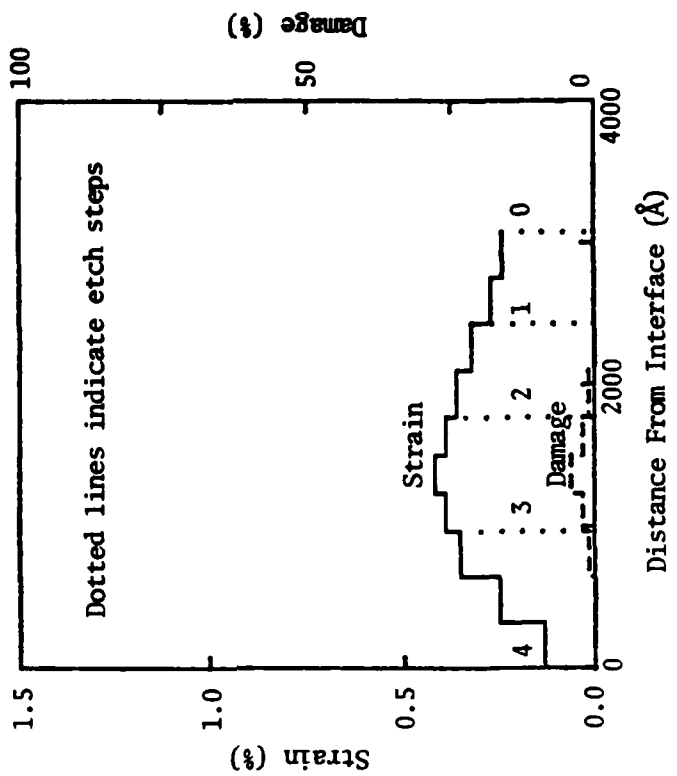
Figure 5. Rocking Curves, and Strain and Damage Distributions for an Implantation of 200 KeV, 6x10^{13} Ne$^+$/cm^2.

14

Although the damage is quite low and the strain is uniform in the cases discussed above, the value of the strain is barely sufficient to overcome the growth-induced anisotropy energy, K_u. Hard-bubble suppression measurements indicate that a substantial increase in the strain is desirable. A three-fold increase is obtained by the 200 KeV, $2 \times 10^{14} Ne^+/cm^2$ implantation shown in Figures 6(a) and (b). The maximum strain here is 1.3 percent, but its distribution is much less uniform, while the damage has increased by much more than a factor of three. Ferromagnetic resonance measurements indicate that for this damage the magnetic properties of the ion-implanted layer are essentially unchanged: $4\pi M_s = 297G$, $\gamma = (1.75 \pm 0.15) \times 10^7/sec\text{-}Oe$, and $\alpha = 0.135 \pm 0.07$ for both the bulk LPE crystal and the implanted layer. The bulk $H_k = 1900 \pm 50$ Oe ($K_u = 22.5$ Kerg/cm^2), while the corresponding value of H_k for the implanted layer is -1090 ± 50 Oe. The implantation-induced anisotropy, $K_i = -35.4$ Kerg/cm^3. Thus, the ratio $K_i/K_u = -1.6$. The relation between K_i and the strain:
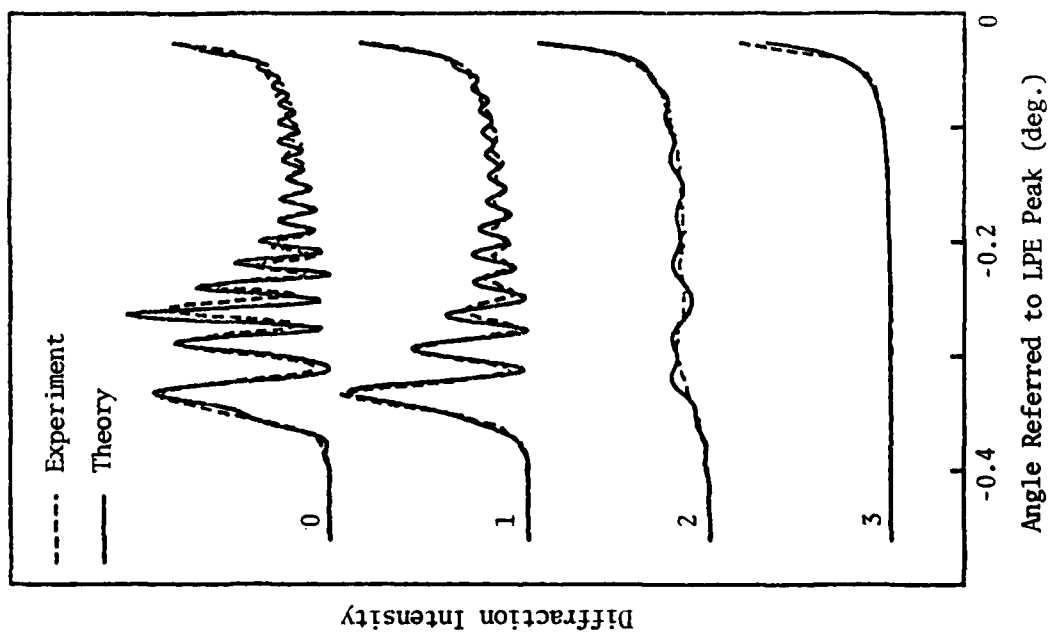
$$K_i = \frac{3}{2} \frac{E}{1+\nu} \lambda_{111} \frac{d-d_o}{d_o} , \qquad (6)$$

yields a value of -1.2×10^{-6} for the magnetostriction constant, λ_{111}. Here Young's modulus, E, and Poisson's ratio, ν, were assumed to be 2×10^{12} and 0.29, respectively. It should be noted that while E and ν are constant for most bubble films, λ_{111} is composition-dependent and can vary by a factor of 2 or 3 in either direction.

Without an increase in λ_{111}, the value of $|K_i|$ cannot be raised significantly by additional implantation. A factor of two increase in the ion dosage, i.e., $4 \times 10^{14} Ne^+/cm^2$, becomes self-defeating since the damage rapidly approaches 100 percent, especially in the middle section of the implanted layer. This is associated with the creation of a nonmagnetic region, about 1500A wide (Ref 19), which does not contribute to the flux-keeper effect or to the charged wall in contiguous disk devices. Further increases in the ion dose result in an entirely nonmagnetic layer. The maximum strain with tolerable damage for Ne^+ implantations is about 1.5 percent.

We return now to the profiles obtained by multiple-energy implantations. The strain and damage distributions resulting from the 200 KeV + 50 KeV, $6 \times 10^{13} Ne^+/cm^2$ for each energy, implantations are shown in Figure 7(b), together with the appropriate rocking curves in Figure 7(a). In the first 2000A from the interface with the bulk, the strain and damage are identical to those obtained by the single 200 KeV, $6 \times 10^{13} Ne^+/cm^2$ implantation. This portion of the implanted layer is unaffected by the 50 KeV implantation. The strain and damage are increased only in the first 1100A from the surface, and the shape of the distribution in this region is qualitatively the same as for a single 50 KeV implantation (except for the presence of a constant positive offset). For this dosage, the contributions of the 50 KeV and 200 KeV implantations are additive, yielding a maximum strain of 0.67 percent and a maximum damage of 11 percent.
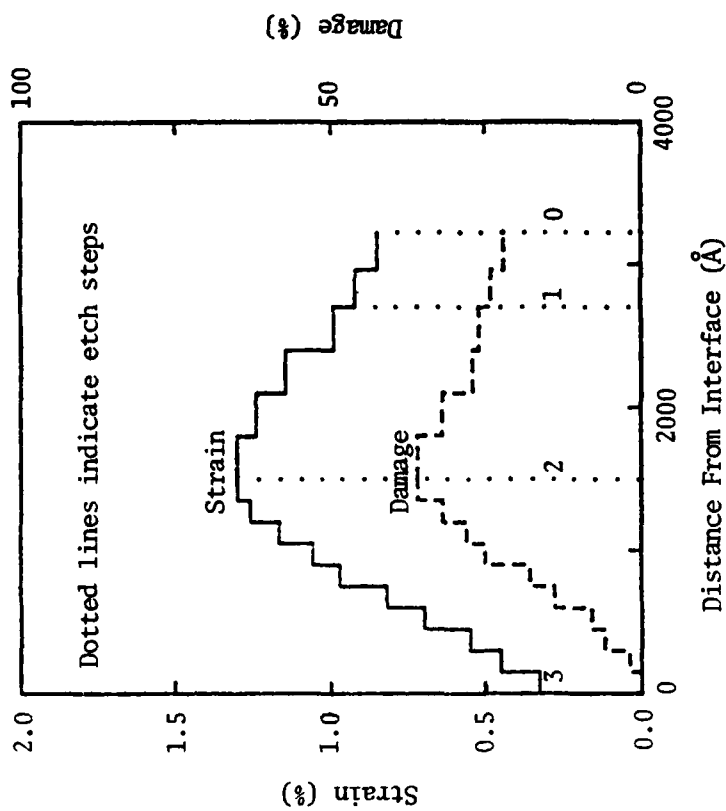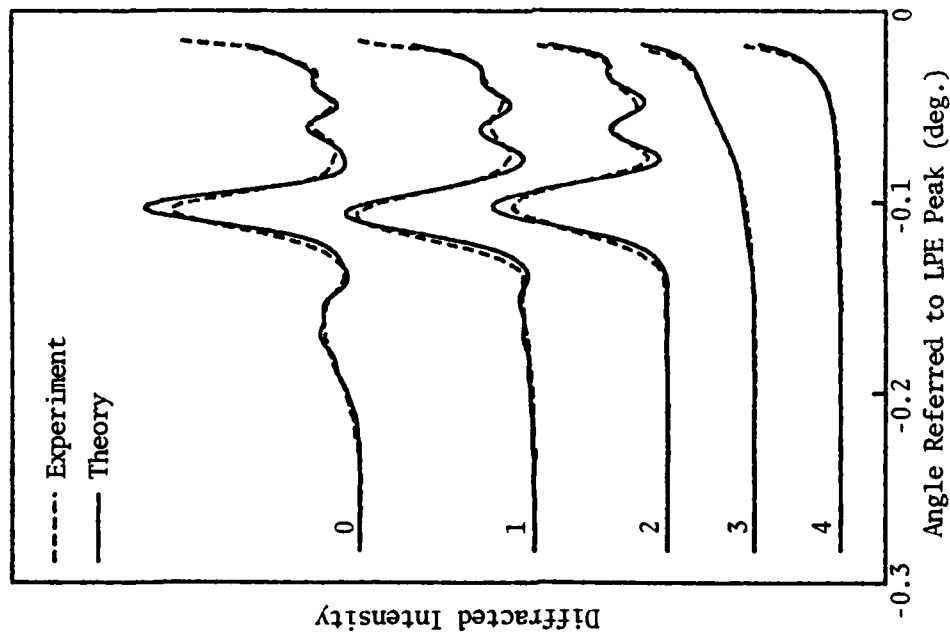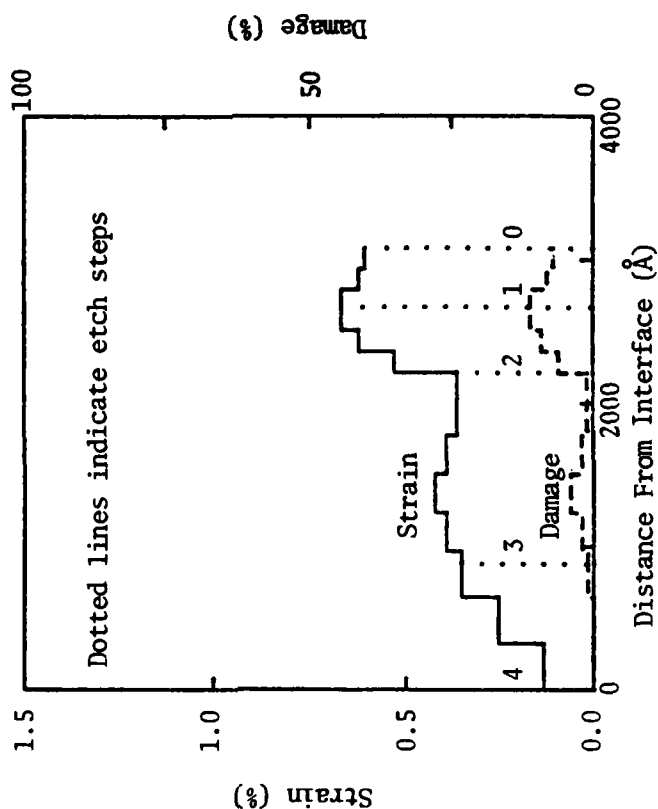
Figure 6. Rocking Curves, and Strain and Damage Distributions for an Implantation of 200 KeV, 2×10^{14} Ne$^+$/cm^2.

(a) Rocking Curves as a Function of Etching

(b) Calculated Strain and Damage Distributions

(b) Calculated Strain and Damage Distributions

(a) Rocking Curves as a Function of Etching

Figure 7. Rocking Curves, and Strain and Damage Distributions for an
Implantation of 200 KeV, 6×10^{13} Ne$^+$/cm^2 and
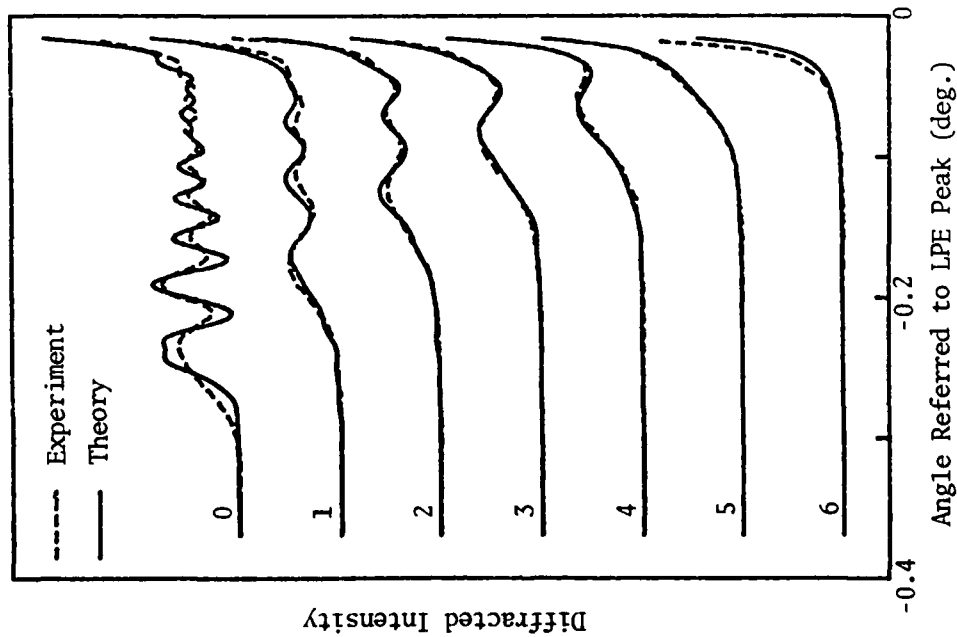50 KeV, 6×10^{13} Ne$^+$/cm^2.

17

The rocking curves of the triple-implanted sample are shown in Figure 8(a). Since the strain and damage distributions for this case were expected to be quite different from the single and double implantations, rocking curves were taken at shorter etch intervals to facilitate the fitting procedure. Here the agreement between experiment and theory is not as good as for the previous cases, consequently there is some uncertainty ($\pm$10 percent) in the distribution in the first 1000$\mathring{A}$ from the surface. An additional rocking curve taken at an etch step of 500$\mathring{A}$ from the surface would have aided in obtaining a better fit.

The strain and damage distributions shown in Figure 8(b) increase almost linearly with distance from the interface up to about 2500$\mathring{A}$. The maximum strain and damage, 1 percent and 31 percent, respectively, indicate that the contribution of each implantation is additive.
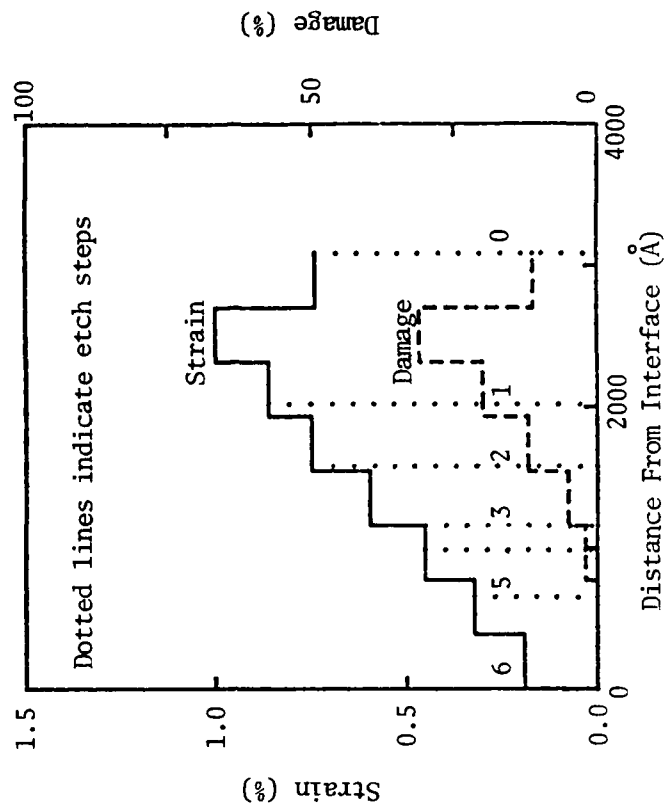
The properties of Ne$^+$-implanted layers can be summarized at this point. The layer thickness increases roughly linearly with ion energy, ranging from 1000$\mathring{A}$ to 3200$\mathring{A}$ for 50 KeV and 200 KeV, respectively. Up to doses of 4×10^{14}Ne$^+$/cm^2, the maximum strain is linear with dosage, but the strain distribution becomes progressively nonuniform. Relatively uniform distributions are obtained by double-energy implantations, such as 200 KeV, 2×10^{14}Ne$^+$/cm^2 + 50 KeV, 6×10^{13}Ne$^+$/cm^2, which yield a strain of 1.3 percent throughout most of the layer. The limiting factor on the useful maximum strain (1.5 percent) is the damage which increases faster than linearly with dosage. For strains less than 1.5 percent, the $4\pi M_s$, γ, α, and the coercivity, H_c, are relatively unaffected by implantation, although the exchange constant, A, is reduced (Ref 14). Depending on the magneto-striction constant, λ_{111}, ratios of 1.5 for K_i/K_u are obtainable.

Contiguous disk devices require an implanted (driver) layer thickness, h_D, to an unimplanted (storage) layer thickness, h_s, ratio of 0.5 to 0.5 (Ref 3). For use with a storage-layer thickness of about 1.5μm, a thicker driver layer is required than 200 KeV Ne$^+$ can produce. For deeper penetration, lighter species, such as He$^+$, H$^+$, or H$_2^+$ are more appropriate, although the dosage required for the same strain can be two orders of magnitude higher. The strain and damage distributions for these species are not the same as for Ne$^+$, and their effect on magnetic properties may be different.

The rocking curves, and the strain and damage distributions for a 60 KeV, 5.5×10^{15}He$^+$/cm^2 implantation are shown in Figures 9(a) and (b). The fit for curve 0 is quite good, but there is a slight phase discrepancy for the remaining curves. This discrepancy corresponds to a 5 percent decrease in the strain distribution after the first etch step. The cause of this is not clear; possibly some annealing occurred during etching at 90°C (for 10 min.) or the removal of the top 700$\mathring{A}$ relieved some of the strain. This effect is occasionally observed in other samples, including Ne$^+$-implanted ones, but its occurrence is erratic. In any case, the strain distribution shown is accurate to 5 percent at any depth.

18

Damage (%)

Dotted lines indicate etch steps

Strain

Damage

Distance From Interface (Å)

Strain (%)

(b) Calculated Strain and Damage Distributions

Experiment
Theory

Angle Referred to LPE Peak (deg.)

Diffracted Intensity

(a) Rocking Curves as a Function of Etching

Figure 8. Rocking Curves, and Strain and Damage Distributions for an
Implantation of 200 KeV, 6×10^{13} Ne$^+$/cm^2 Plus
120 KeV, 6×10^{13} Ne$^+$/cm^2 and 50 KeV, 6×10^{13} Ne$^+$/cm^2.
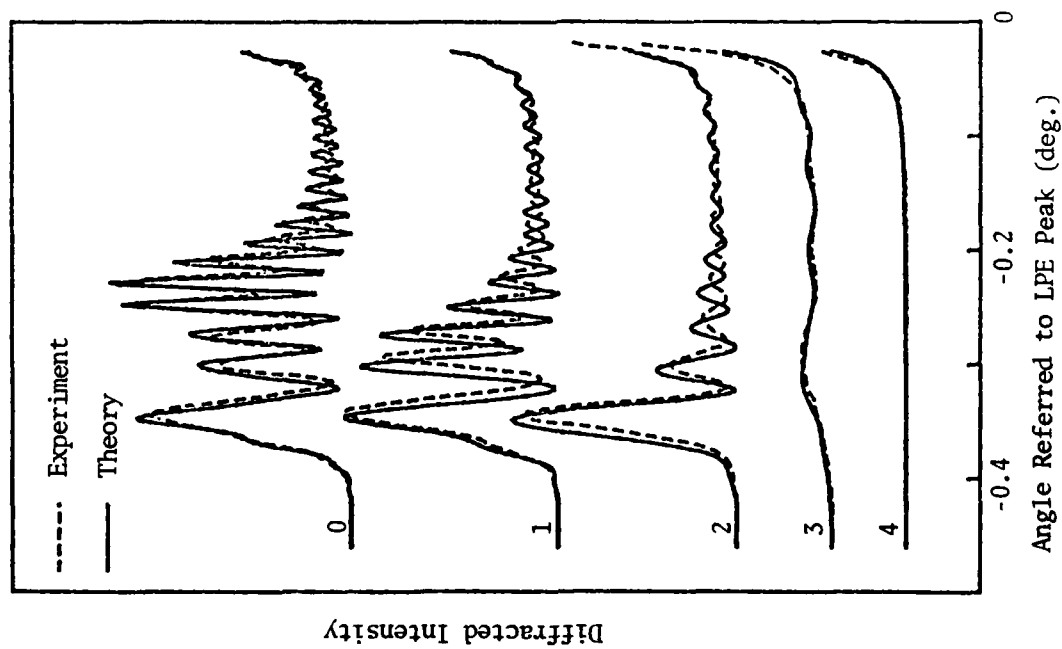
(b) Calculated Strain and Damage Distributions

(a) Rocking Curves as a Function of Etching
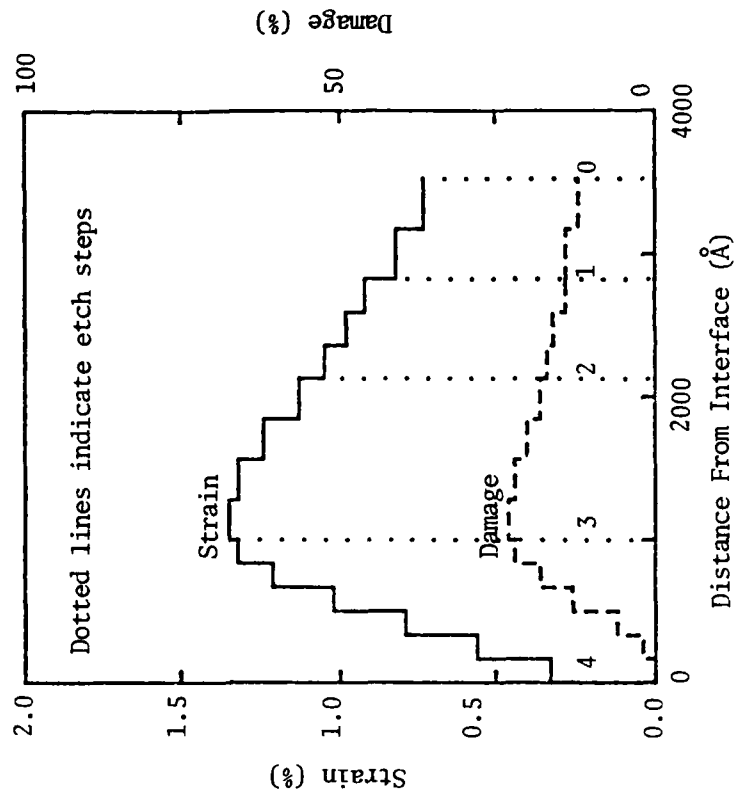
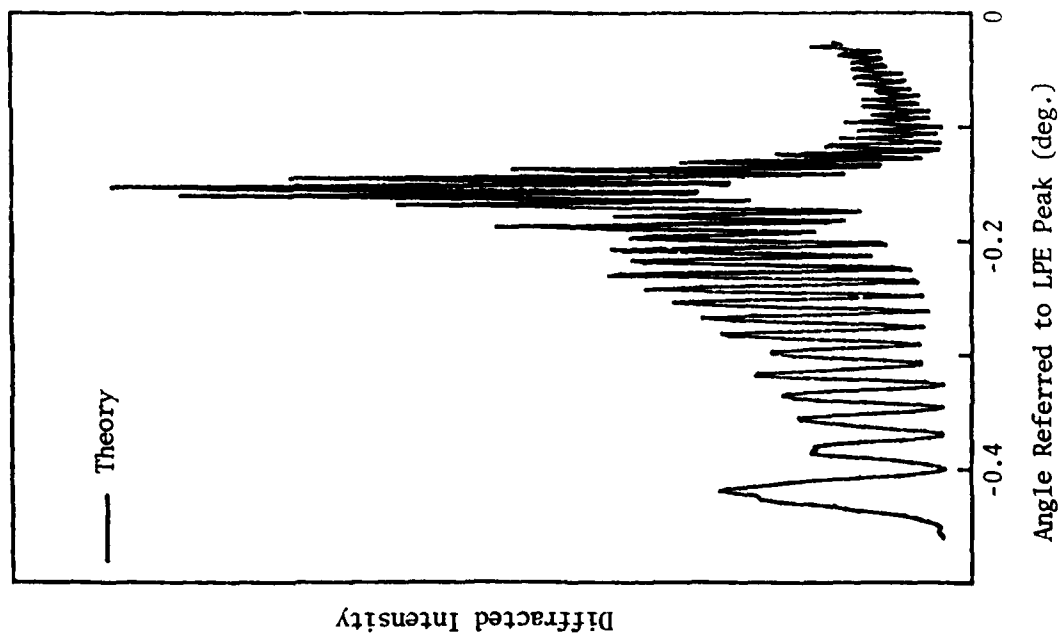Figure 9. Rocking Curves, and Strain and Damage Distributions for an Implantation of 60 KeV, 5×10^{15} He^+/cm^2.

20

For this dosage and energy, the layer thickness and maximum strain are comparable to the 200 KeV, $2\times10^{14}Ne^+$ implantation. The strain distribution is slightly more skewed and less uniform. Although there is a ±10 percent uncertainty in the damage distribution, its peak value is about 50 percent less than for Ne^+. This result is important to the physics of ion-lattice interaction, but within the resolution of our measurements, does not affect the garnet's magnetic properties differently. The values for $4\pi M_s$, γ, α, and H_k are essentially the same as obtained for Ne^+.

The penetration depth of 200 KeV He^+ ions in garnet is 0.75µm, as shown in Figure 10(b). The dosage is $1\times10^{16}He^+/cm^2$, resulting in 1.6 percent maximum strain and 46 percent maximum damage. Note that the distance scale has been increased by a factor of 2, so that the distribution is not significantly more peaked than that shown in Figure 9(b). The rocking curve in Figure 10(a) is theoretical, but the agreement with experiment is reasonably good. The uncertainty in the distributions is not more than ±10 percent. It is clear from the strain distribution that multiple energy implantations are necessary in order to obtain a uniformly strained layer.

Ion-implantation depth is roughly proportional to the ion-accelerating voltage and to the reciprocal of the mass of the implanted ion. Thus, the implanted layer thickness for 200 KeV Ne^+, He^+, and H^+ was found to be 0.32, 0.75, and 1.25µm, respectively. The implantation-induced strain and damage are approximately symmetrically distributed through the implanted layer for Ne^+ but are skewed toward the end of the penetration range for lighter ions.

Despite the need for deeper implantations, studies on H^+-implanted garnets have not been very numerous because of the high dosage needed, and the lack of a suitable etchant. For a strain of about 0.4 percent, the dosage requirements at 200 KeV are $6\times10^{15}Ne^+/cm^2$, $1.5\times10^{15}He^+/cm^2$ and $2\times10^{16}H^+/cm^2$. The durations of implantation for He^+ and H^+ are therefore about 25- and 300-times that for Ne^+ at the same ion-beam current. Higher ion-beam currents may be employed to reduce the light-ion implantation time (within equipment limitations), but an accompanying rise in wafer surface temperature produces self-annealing which is counterproductive to increasing strain. In order to analyze the strain and damage distributions by the techniques developed for Ne^+-implantations, a uniformly-acting slow etchant is required. Unfortunately, hot HNO_3 attacks H^+-implanted material unevenly, producing a roughened surface so that successive rocking curves cannot be prepared. It is possible to compare the as-implanted rocking curves of Ne^+- and H^+-implanted garnets to obtain the maximum strain, and estimates of the strain and damage distributions in the H^+-implanted material. Detailed measurements however must await the development of a suitable etching technique.

Our results indicate that uniformly strained layers with appropriate thickness, magnetic properties and low damage can be produced by double- or triple-energy implantations of Ne^+ and He^+. Since the dosage requirements for H^+ exceed those for He^+ by five-fold, H^+ implantation is less attractive.
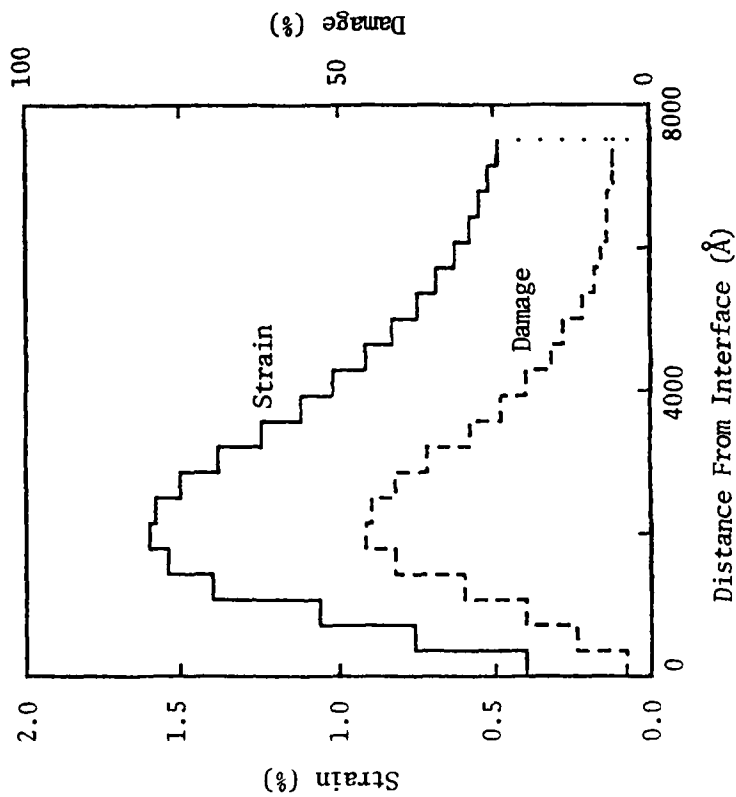
Figure 10. Calculated Rocking Curve, and Strain and Damage Distributions
for an Implantation of 200 KeV, 1×10^{16} He$^+$/cm^2.

(a) Calculated Rocking Curve

(b) Calculated Strain and Damage Distributions

22

SECTION IV

CONCLUSIONS

A method for using X-ray diffraction to study ion-implanted crystals has been described. Strain and damage distributions in bubble garnets for single energy, and in some cases multiple energy, Ne^+, He^+, and H^+ implantations were discussed. Sufficiently uniform strains of appropriate values (1.0 to 1.5 percent) are obtainable by multiple energy, dosage, and/or species implantation. The maximum usable strain is limited by the damage, which increases rapidly for strains over about 1.5 percent. For low (≤ 35 percent) damage, the magnetic properties of the garnet are essentially unchanged, except for the creation of the stress-induced anisotropy energy, K_i. This parameter is proportional to the product of the strain and the magnetostriction constant, λ_{111}. For contiguous disk device applications, the value of K_i should exceed the growth-induced anisotropy K_u by $\gtrsim 50$ percent. Ferromagnetic resonance measurements on 1.5μm-diameter bubble materials indicate values of about 50 Kerg/cm^3 and about 75 Kerg/cm^3 for the K_u and K_i, respectively.

As the bubble size is decreased for higher bit densities, both $4\pi M_s$ and K_u increase, making it more difficult to create a K_i of sufficient magnitude. The composition-dependent λ_{111} could be raised to meet this problem, but compositional changes affect other magnetic parameters including K_u. Thus for smaller bubble material, it may be necessary to resort to double-layered films that have a driver layer with a low K_u (which can be exceeded by K_i). However, fabrication costs for double-layer films will be higher than for single-layer films, and the possibility of defect formation will increase. Another aspect of smaller-bubble material is that the required thickness of the implanted layer also decreases, making a single- or double-Ne^+ implantation suitable.

A more complete understanding of implanted layer properties should result from the use of additional observation techniques. Ferrofluid decoration would permit estimation of the strength and length of the charged wall, and this information could be correlated to the driver layer thickness, strain, and damage. In addition, independent determination of λ_{111} by FMR on unimplanted, externally-stressed samples would aid in determining the potential of a material for a high K_i prior to implantation.

REFERENCES

1. B. L. Crowder, ed., "Ion-implantation in Semiconductors and Other Materials," Plenum Press, New York, 1973.

2. R. Wolfe and J. C. North, Bell Syst. Tech. J. 51, 1436 (1972).

3. Y. S. Lin, G. S. Almasi, and G. E. Keefe, J. Appl. Phys. 48, 5201 (1977).

4. W. A. Johnson, J. C. North, and R. Wolfe, J. Appl. Phys. 44, 4753 (1973).

5. R. F. Soohoo, J. Appl. Phys. 49, 1582 (1978).

6. J. P. Omaggio and P. E. Wigen, J. Appl. Phys. 50, 2264 (1979).

7. J. Engemann and T. Hsu, Appl. Phys. Lett. 30, 125 (1977).

8. J. W. Mayer, L. Eriksson, S. T. Picraux, and J. A. Davies, Can. J. Phys. 46, 663 (1968).

9. G. H. Schwuttke, "Crystal Properties as Influenced by Crystallographic Imperfections," AFCRL-72-0176, 15 February 1972, Contract No. F19628-71-C-0095.

10. D. Taupin, Bull. Soc. Franc. Miner. Crist., 87, 469 (1964).

11. A. Fukuhara and Y. Takano, Acta Cryst. A33, 137 (1977).

12. K. Komenou, I. Harai, K. Asama, and M. Sakai, J. Appl. Phys. 49, 5816 (1978).

13. V. S. Speriosu, H. L. Glass, and T. Kobayashi, Appl. Phys. Lett. 34, 539 (1979).

14. C. H. Wilts, J. Zebrowski, and K. Komenou, J. Appl. Phys. 50, 5878 (1979).

15. R. W. James, Solid State Phys. 15, 132 (1963).

16. A. M. Afanasev, M. V. Kovalchuck, E. K. Kovev, and V. G. Kohn, Phys. Status Solidi A42, 415 (1977).

17. R. W. James, "The Optical Properties of the Diffraction of X-rays," Cornell University Press, Ithaca, N.Y. 1965.

18. R. Wolfe, J. C. North, and Y. P. Lai, Appl Phys. Lett. 22, 683 (1973).

19. K. Komenou, J. Zebrowski, and C. H. Wilts, J. Appl. Phys. 50, 5442 (1979).

DATE
ILMED

-8